THE UNIVERSITY *of* EDINBURGH

Edinburgh Research Explorer

On the Trade-off Between Spatial Resolution and High Curvature Bending in FBG-based Shape Sensing.
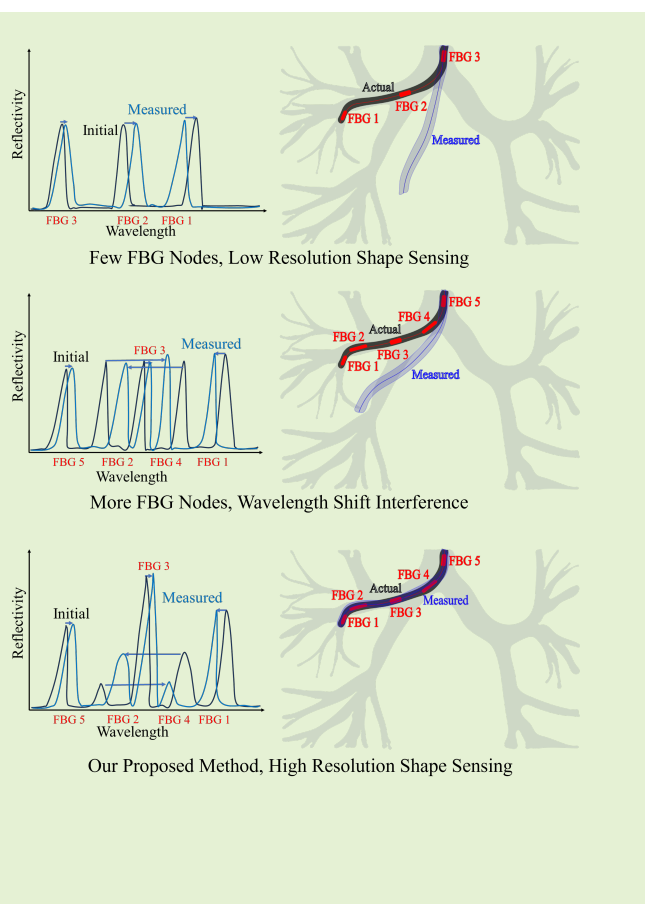
OPEN ACCESS

On the Trade-Off Between Spatial Resolution and High Curvature Bending in FBG-based Shape Sensing

David Hanley[1] and Kevin Dhaliwal[2] and Mohsen Khadem[1]

Abstract—Fiber Bragg grating (FBG)-based shape sensing is an emerging technology used for the navigation of flexible medical instruments, such as needles, catheters, and endoscopes. FBG-based sensors operate by measuring strain-induced wavelength shifts in the reflected light, which are used to determine the curvature along a fiber's length. While an increased number of gratings enhances shape-sensing accuracy, incorporating many within a fixed spectrum can induce interference in wavelength shifts, specifically during high curvature bending, limiting the detectable bending range. Such interference severely compromises shape estimation, posing challenges for instruments requiring high curvature bends. In this paper, we study this trade-off between resolution and bending curvature. Next, we introduce an algorithm that leverages the reflectivity and full-width half maximum of FBG nodes for improved bend estimation, even in high-curvature scenarios. To this end, first, we provide a model of reflectivity of uniform gratings using coupled-mode theory. The model is used to match spectrum measurements with FBG nodes. Second, we develop an algorithm using the proposed model and random walk model to estimate the relative probability of a given reflected wavelength corresponding to each FBG node. This algorithm then uses variants of the Hungarian algorithm to solve an assignment problem and classify FBG nodes. We then collected three datasets with FBGs experiencing varying curvature. One of the datasets validates the proposed model and the latter two demonstrate that, relative to a commercially available interrogator, our approach classifies FBG nodes with 14% higher accuracy, 13% higher precision, 35% higher recall, and 4% higher specificity.

Index Terms—Shape Sensing, Fiber Bragg Gratings, Coupled-mode Theory

Few FBG Nodes, Low Resolution Shape Sensing

More FBG Nodes, Wavelength Shift Interference

Our Proposed Method, High Resolution Shape Sensing

I. Introduction

FIBER Bragg Grating (FBG) shape sensing is a technology that uses optical fibers embedded with Bragg gratings to monitor the real-time three-dimensional shape/position of objects in motion. This approach serves as an alternative to traditional shape-sensing methods and offers several advantages,

such as minimal footprint, large sensing length, high strain sensing accuracy, and the ability to perform dynamic sensing. FBG-based shape sensing has enabled unique advances in various navigation tasks, such as tracking robots and medical instruments (needles, catheters, and endoscopes) inside the human body [1]. The use of FBGs in shape estimation go beyond tracking medical instruments. This technology has applications to tracking the deformations of structural components such as carbon fiber reinforced polymers and structural health monitoring more generally [2], [3].

FBGs allow shape estimation of a flexible instrument by measuring strain on various points along its arclength. These fibers are engineered to feature a periodic variation in refractive index at specific locations, known as Bragg gratings. As

[1]David Hanley and Mohsen Khadem is with the School of Informatics and the Translational Healthcare Technologies Group in Centre for Inflammation Research, Institute for Regeneration and Repair, University of Edinburgh, UK, {dhanley,mohsen.khadem}@ed.ac.uk

[2]Kevin Dhaliwal is with the Translational Healthcare Technologies Group in the Centre for Inflammation Research, Institute for Regeneration and Repair, University of Edinburgh, UK, kev.dhaliwal@ed.ac.uk

light traverses the fiber, each Bragg grating reflects a particular wavelength. Any strain experienced at the FBG node induces a corresponding shift in this reflected wavelength. To detect this strain, an interrogator device introduces light into the optical fiber and subsequently analyzes the shifted reflected wavelength. This shift directly corresponds to the strain the FBG node undergoes [4].

Three or more FBGs can be used to measure directional strain along a flexible instrument and reconstruct its 3D shape [5]–[7]. Alternatively, a single multi-core fiber with multiple Bragg gratings can be used to remove the need to manually position the fibers [8], [9]. This enables real-time monitoring of the 3D shape and position of the object to which the fiber is attached.

One of the drawbacks of FBG shape sensing is the number of measurement points readable in a common fiber path [9]. The spatial resolution of shape estimation–i.e., accuracy in curvature estimation along fiber arclength–improves with an increased number of FBG nodes along the length of the fiber. However, increasing the number of FBG nodes increases the probability of wavelength shifts interfering with each other, especially during high curvature bending where wavelength shifts are relatively large. This results in a wavelength classification problem for the interrogator. An FBG wavelength shift can be missed or classified as belonging to an incorrect FBG node. This results in poor shape estimates. This trade-off is particularly problematic in shape sensing of flexible medical instruments, where precise shape sensing is crucial. Specifically, endoscopes that are relatively long and undergo large deflections can suffer from these problems.

To address this issue, several researchers have fused FBG-based sensing methods with other sensing modalities to provide more accurate and reliable shape sensing. In [10], two algorithms, namely, a Luenberger observer and Kalman filter, are used to track the tip of a magnetically actuated catheter. Both estimators combine FBG shape sensing and ultrasound tracking. A similar approach was implemented in [11] to track the tip of a continuum manipulator in a 2D plane with a Kalman filter, combining FBG sensors and simulated low radiation fluoroscopy imaging. Similarly, fusing FBG-based shape estimates with biplane fluoroscopy imaging has been used in [12]. In [13], FBG measurements are fused with electro-magnetic sensing to optimize the control points of a Bézier curve for shape estimation. In [14], FBG sensors are used in conjunction with both an electromagnetic tracker and an intravascular ultrasound for shape sensing.

One area of prior work that has been used to address this issue is the design of a line of interrogators and FBG nodes to apply principles of code division multiplexing. FBG nodes designed as discrete prolate spheroidal sequences were used for multiplexing [15]. In another work, researchers designed nodes as super-structured FBGs to create codes for multiplexing [16]. Throughout this work, we use FBG nodes without these types of codes embedded and we use an interrogator meant for wavelength division multiplexing as opposed to code division multiplexing.

Another line of prior work has proposed using deep learning to classify multiplexed FBGs along an optical fiber and esti-

mate wavelength shift with higher accuracy. Such methodologies treat raw wavelength signals aiming to discern wavelength shifts and, consequently, estimate fiber shape, approaching the issue as an end-to-end blackbox problem. In [17], a neural network is proposed to classify and estimate wavelength shift of FBG nodes for shape estimation. In [18], a gated recurrent unit (GRU) based neural network is used to perform intensity wavelength division multiplexing on an FBG sensor array in a ring structure.

To improve shape sensing resolution in high curvature bendings, researchers rely on other sensors that can be expensive, have low temporal resolutions, and are difficult to use [19]. The deep learning approaches, while promising, often require extensive training datasets. Moreover, these models lack interpretability, making it challenging to generalize their shape estimation to unseen realistic clinical scenarios.

In this paper, we hypothesize that other signal features like full-width half maximum (FWHM) or reflectivity of FBG nodes (i.e, percentage of the intensity of light reflected back at a given wavelength) can be used to improve the classification of FBG nodes even during high curvature bends with wavelength interference. Therefore, effectively resolving the trade-off between spatial resolution and bending curvature. To this end, we

1. Present a model of reflectivity for uniform FBG nodes as a function of varying FWHM using coupled-mode theory.
2. Present a new classification algorithm that employs the model to assign wavelength shifts to corresponding nodes during high curvature bending with interfering wavelengths.
3. Evaluate the model and classification method on a dataset and demonstrate superior performance relative to a commercially available interrogator.

The model and classification method combined can, with a relatively small amount of training data, allow FBG nodes to cross on spectrum and thereby provide opportunities to use many nodes for high-resolution shape sensing during high curvature bending.

We describe in mathematical terms the spatial resolution vs. high curvature bending trade-off in Section II. In Section III, we present our methodology for resolving this trade-off, which includes presenting the reflectivity model—beginning with basic equations from coupled-mode theory—followed by how we use this model for FBG node classification. We demonstrate the efficacy of this approach through experiments described in Section IV. Concluding remarks and discussion of limitations appear in V.

II. SPATIAL RESOLUTION VS. HIGH CURVATURE BENDING

In this section, we point out the limitations on shape sensing that occur when many nodes are placed along the fiber to improve the spatial resolution of shape sensing. Specifically, when wavelength peaks are not able to cross on an interrogator's spectrum. First, we describe the relationship between two separate FBG node's design wavelengths and bending curvatures. Then, we illustrate the problem that occurs

with shape sensing during high curvature bendings on an example. Finally, we illustrate the potential benefit of resolving this trade-off between spatial resolution and high curvature bending.

Assume two uniform FBG nodes with design Bragg wavelengths $\lambda_{B,1}$ and $\lambda_{B,2}$ where $\lambda_{B,2} > \lambda_{B,1}$. Note the difference between the two wavelengths as $\delta\lambda_B = \lambda_{B,2} - \lambda_{B,1}$. When an FBG experiences strain, its Bragg wavelength shifts by $\Delta\lambda_B$ and the new wavelength is $\lambda_B + \Delta\lambda_B$. The wavelength-strain relation for a single mode SMF28 fiber is

$$\Delta\lambda_B = 0.79\epsilon\lambda_B \tag{1}$$

where ϵ is the strain experienced by the FBG node [20]. When optical fibers with FBG nodes are laid along a rod in parallel, their strain-curvature relation is

$$\epsilon = -\kappa r \sin(\phi + \gamma) + \epsilon_0 \tag{2}$$

where κ is the curvature, r is the radius of the rod, ϕ is the bending angle, γ is the orientation of the FBG node on the rod, and ϵ_0 is a residual strain on the FBG node [7]. Assuming no residual strain and that curvature corresponds to the maximum possible strain on the FBG node (e.g., $\phi + \gamma = \frac{\pi}{2}$), we can relate the wavelength to curvature with the relation

$$\Delta\lambda_B = -0.79\lambda_B\kappa r. \tag{3}$$

We are interested where the Bragg wavelengths may cross. In other words, where

$$\Delta\lambda_{B,1} - \Delta\lambda_{B,2} > \delta\lambda_B. \tag{4}$$

Using the curvature-wavelength relation we simplify by plugging (3) in for each FBG's $\Delta\lambda_B$ and then use the definition of $\delta\lambda_B$ to eliminate $\Delta\lambda_{B,2}$. We arrive at the relation for the region of design Bragg wavelength difference that will not be admissible due to interference, if $0.79r\kappa_2 - 1 < 0$,

$$-\frac{0.79r\lambda_{B,1}(\kappa_2 - \kappa_1)}{0.79r\kappa_2 - 1} > \delta\lambda_B \tag{5}$$

or, if $0.79r\kappa_2 - 1 > 0$,

$$-\frac{0.79r\lambda_{B,1}(\kappa_2 - \kappa_1)}{0.79r\kappa_2 - 1} < \delta\lambda_B. \tag{6}$$

Note that as the difference between curvatures at two FBG nodes $(\kappa_2 - \kappa_1)$ grows, so does the required initial difference in Bragg wavelengths $\delta\lambda_B$ to prevent interference. This is a restriction on shape sensors that can be challenging, particularly for medical endoscopes/bronchoscopes where the curvatures can vary significantly.

Of course, interference of two Bragg wavelengths do not occur just when two Bragg wavelengths cross. This is because each FBG node reflects light over a range of wavelength, creating a bump on the interrogator's spectrum with notable width as well as a peak at the Bragg wavelength. Given two FBG nodes of widths w_1 and w_2, the admissible region, if $0.79r\kappa_2 - 1 < 0$, becomes

$$-\frac{0.79r\lambda_{B,1}(\kappa_2 - \kappa_1) - w_1/2 - w_2/2}{0.79r\kappa_2 - 1} > \delta\lambda_B \tag{7}$$
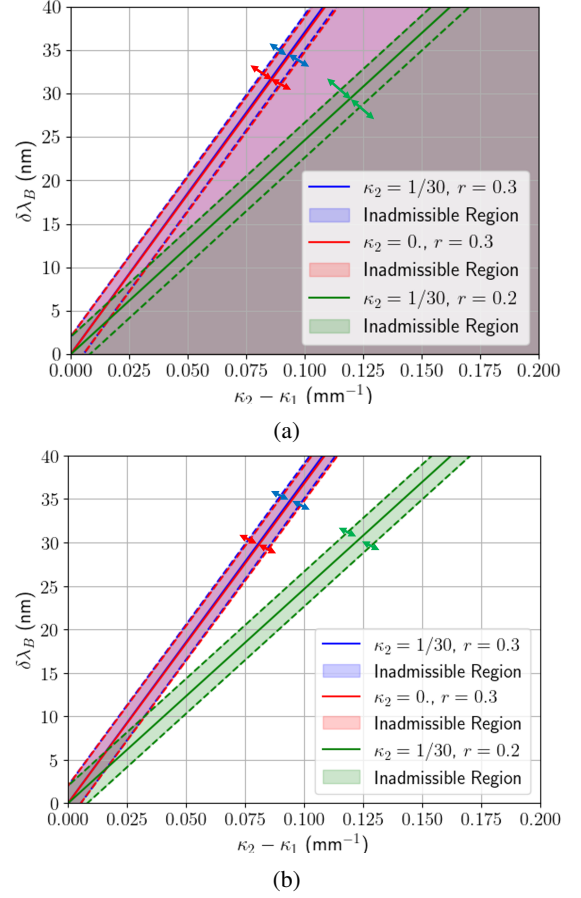

Fig. 1: A comparison of admissible measurements due to wavelength shift interference (a) with and (b) without the proposed method. (a) Inadmissible curvature measurements are shown with shaded colors as a function of the differences in the curvature of the two consecutive FBG nodes. Results for different κ_2 (curvature at node 2), radius of the rod (r) on which the FBG is laid, and the width of the FBGs on the interrogator's spectrum is shown. (b) Inadmissible regions are shaded as a function of the differences in the curvature of the two nodes using our proposed approach.

or, if $0.79r\kappa_2 - 1 > 0$,

$$-\frac{0.79r\lambda_{B,1}(\kappa_2 - \kappa_1) - w_1/2 - w_2/2}{0.79r\kappa_2 - 1} < \delta\lambda_B. \tag{8}$$

Note that while w_1 and w_2 can vary, we do not derive any direct relation to difference in curvature $(\kappa_2 - \kappa_1)$ or difference in the initial Bragg wavelength $(\delta\lambda_B)$ here. Moreover, we did not see an obvious relation between these variables experimentally.

To illustrate the spatial resolution vs. high curvature trade-off more concretely and to illustrate the impact our method has on the admissible region of shapes, we perform a simulation study. Given an FBG array with two nodes laid on a rod with a radius of 0.3 mm and center wavelength of 1550 nm for FBG 1 (roughly the center of the measured spectrum of the interrogator used in experiments in Section IV). Assume FBG 2 has a curvature of 3.0 cm^{-1}. Also, assume both wavelengths have a width of 1.0 nm. Fig. 1a shows the initial difference in wavelengths between the two FBG nodes ($\delta\lambda_B$) that would

make this shape (defined by $\kappa_2 - \kappa_1$) admissible. Again, note that these regions are not static over time because width of FBGs on an interrogator's spectrum can change. This is visualized on the plot with colored arrows which change the offset of the dashed lines (corresponding to the left edge of one FBG crossing the right edge of another FBG and vice versa). Fig. 1a also shows the admissible region for the case where a rod with a smaller radius of 0.2 mm is used and where FBG 2 has no initial curvature ($\kappa_2 = 0$). Note that most of the visualized region is actually inadmissible. Fig. 1b on the other hand shows the inadmissible region when using the proposed method to estimate wavelength shift. Note how in this case, only a small proportion of the visualized area is inadmissible.

As a further illustration of the above result, consider the same case above with a rod with radius 0.3 mm and FBG 1 at 1550 nm and FBG 2 at 1560 nm (i.e., $\delta\lambda_B$ is 10 nm). Assume the system follows an s-curve shape with radii of curvature of ± 3 cm as shown in Fig. 2. Assuming uniform FBG nodes with length 2 mm and uniform gratings as described in [21] with effective refractive index 1.5 and a constant effective refractive index change spatially averaged over a grating period of 1×10^{-4} (details of these variables described in more detail in Section III), we can simulate the spectrum as shown in Fig. 2. The same spectrum prior to bending is also shown. As can be seen, the peak reflectivity of the two peaks switch order which can lead to incorrect classification. The result of incorrect classification is a substantially incorrect shape estimate. In the 2D example shown, the estimated radius curvature resulting from an incorrect classification is 15.8 cm and 16.5 cm for the simulated FBGs respectively. Fig. 2 illustrates the incorrect shape estimate as dashed lines.

III. METHODOLOGY

Fig. 3 shows an overview of the process we use for peak detection and classification described in this paper. This method depends on varying the FWHM and reflectivity of FBG nodes to create identifiable spectra and associated models. In subsection III-A, we use coupled-mode theory to develop a model of FBG nodes with different design FWHM and peak reflectivity. Then we present our method for detection and classification in subsections III-B and III-C respectively.

A. Coupled-Mode Theory and Model of Reflectivity

In this section, we use coupled-mode theory to develop a model of FBG nodes' peak reflectivity as a function of design FWHM. As the node experiences strain, the FWHM and peak reflectivity will vary. We aim to model this variation and later leverage it for peak classification during high curvature bends. The model is developed assuming a uniform grating.

Uniform fiber Bragg gratings have a maximum reflectivity (r_m) described by [21]

$$r_m = \tanh^2\left(\frac{\pi v L}{\lambda_{\max}}\right) \qquad (9)$$

where v is the fringe visibility parameter of the index changes in the FBG (for uniform gratings, this is usually assumed to be equal to 1), L is the length of the FBG node, and $\lambda_{\max}$ is
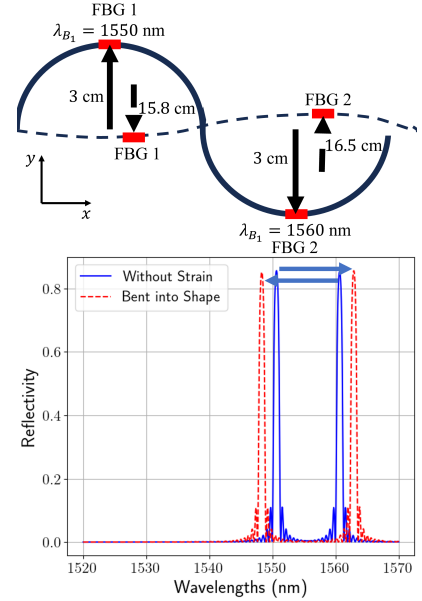

Fig. 2: An example case with FBGs following an s-curve with spectrum modelled with the coupled-mode theory of [21]. Results show that the s-curve causes the FBG peak reflectivities to switch order resulting in confusion during classification. Incorrect classification leads to major shape errors as shown by the dashed line. The arrows show actual changes in wavelengths.

the wavelength at which maximum reflectivity occurs, given by [21]

$$\lambda_{\max} = \left(1 + \frac{\overline{\delta n_{eff}}}{n_{eff}}\right)\lambda_B \qquad (10)$$

where n_{eff} is the effective refractive index of the fiber. Due to the grating pattern, the effective refractive index varies regularly along the length of the grating. The variable $\overline{\delta n_{eff}}$ is the constant effective refractive index change spatially averaged over a grating period (often called the DC index change due to it being analogous to the DC component of an alternating signal), and λ_B is the Bragg wavelength. The FWHM of a uniform FBG has been shown to be [20]

$$FWHM = \lambda_B S \xi \qquad (11)$$

where

$$\xi = \left(\left(\frac{v\overline{\delta n_{eff}}}{2(n_{eff} + \overline{\delta n_{eff}})}\right)^2 + \left(\frac{1}{N}\right)^2\right)^{\frac{1}{2}} \qquad (12)$$

and where S is a parameter of the grating that is approximately equal to 1 for high reflectivity grating and 0.5 for weak reflectivity gratings and N is the number of periods on an FBG node.

Now, to find the relationship between the maximum reflectivity and FWHM we can replace the Bragg wavelength with the maximum wavelength

$$FWHM = \frac{\lambda_{\max} n_{eff} S \xi}{n_{eff} + \overline{\delta n_{eff}}} \qquad (13)$$
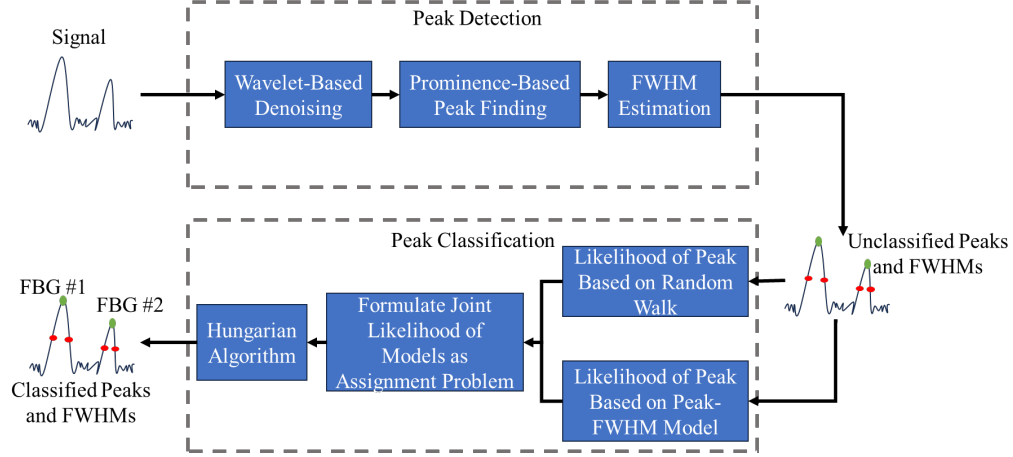
Fig. 3: The peak detection and classification process used based on the relationship between varying reflectivity and FWHM of FBGs.

and then solving for the maximum wavelength and plugging into (9) we get

$$r_m = \tanh^2\left(\frac{\pi v \overline{\delta n_{eff}} n_{eff} LS\xi}{FWHM\left(n_{eff} + \overline{\delta n_{eff}}\right)}\right). \quad (14)$$

Note that in the equation above, as an FBG grating experiences strain, the length L must change. We also generally expect the FWHM and reflectivity to change. We assume a relationship between length and FWHM, and we assume that relationship is analytic. However, given that this relationship is not currently known, we choose to represent it by the first two elements of its power series

$$L = f(FWHM) \approx c_0 + c_1 FWHM. \quad (15)$$

Plugging this into the above equation, we can simplify to a function of two parameters

$$r_m = \tanh^2\left(\frac{\alpha\pi}{FWHM} + \beta\right). \quad (16)$$

We use this model throughout the paper for FBG modeling and classification.

B. Peak and FWHM Detection

Measurements made from a FBG interrogator can be noisy (depending on model used), therefore, we use a peak detection process similar to methods used in fields such as mass spectrometry [22], [23]. In keeping with these prior methods, we first take the undecimated discrete wavelet transform (UDWT) of the signal. We choose to use eighth order Daubechies wavelets and we use hard thresholding to eliminate all wavelet coefficients below some multiple of the mean average deviation of the coefficients. An inverse UDWT is then used to create a new denoised signal.

Peaks are computed on the denoised signal using a minimum prominence threshold. Topographic prominence is the height of a peak over its lowest contour line, but without containing a higher peak within it. This process helps to eliminate extraneous peaks created with the FBGs (due to a non-uniform strain for example).

The FWHM for each peak is computed on the original signal source by successively stepping to the left and right of each computed peak until the half maximum (with respect to some minimum baseline of the signal) is found. In the event a half maximum is not found (i.e., the first or last measurement of the sensing window is reached) then the detected peak is removed. If the leftward search crosses a second peak before finding the half maximum point, then the wave is assumed to be symmetric and FWHM is computed using only the half maximum found to the right of the peak (and vice versa). If more than one peak is crossed before locating the half maximum on the left or right side, then the measured peak and FWHM is taken to be too ambiguous and removed. The end result of this process is a list of peaks, FWHM, and their corresponding wavelengths.

C. Peak Classification

Given a set of peaks, FWHMs, and their associated wavelengths identified, our objective is to associate each identified peak with a known FBG node. It is also possible that a peak that is identified may not be associated with any known FBG node and, likewise, a known FBG node may not have a peak identified with it at any given point in time. This can occur in particular when the FBG nodes interfere (i.e., their peaks occur at very similar wavelengths) or when an FBG node experiences stresses that move the peak wavelength beyond the range of the interrogator. In general, we believe that it is preferable to leave a given peak measurement unmatched with an FBG node at any given point in time than to associate it with the incorrect FBG node. The logic for this preference is grounded in the fact that there are established ways to deal with uncertainty in robotic state estimation, planning, and control. However, significantly incorrect measurements with high certainty is problematic and more challenging to deal with.

We formulate this problem as an assignment problem with M being the number of possible assignment for measured peaks. The variable M is equal to the number of known FBG nodes plus the number of measured peaks (which could all be left unassigned to known FBG nodes in an extreme case). We

define N_R as the number of measured FBG peaks (therefore, $M \geq N_R$). The assignment problem then is

$$\mathbf{x}^* = \arg\min_{\mathbf{x}} \sum_{i=1}^{N_R} \sum_{j=1}^{M} c_{i,j} x_{i,j} \qquad (17\text{a})$$

$$\text{subject to} \quad \sum_{j=1}^{M} x_{i,j} = 1 \quad \forall i \qquad (17\text{b})$$

$$\sum_{i=1}^{N_R} x_{i,j} \leq 1 \quad \forall j \qquad (17\text{c})$$

$$x_{i,j} \in \{0,1\}. \qquad (17\text{d})$$

Here $x_{i,j}$ is a binary assignment variable where 1 is defined as corresponding to when peak measurement i is associated with known (or unassigned) FBG node j and $x_{i,j}$ is 0 otherwise. The variables $c_{i,j}$ is a cost associated with matching peak measurement i associated with known (or unassigned) FBG node j. The variable $\mathbf{x}^*$ is a matrix of optimal binary assignment variables where rows correspond to peak measurements and columns correspond to the known (or unassigned) FBG nodes. An established solution to this type of problem is the Hungarian algorithm and its variants [24], [25].

Note that in the prior subsection, interrogator measurements of the spectrum can be used directly (in terms of intensity and wavelength, for example). Here, however, we assume interrogator measurements have been converted into a set of wavelengths and reflectivity.

The costs in our particular assignment problem is determined by computing the likelihood of peak measurements given prior measurements and models of the peak as a function of FWHM. The likelihoods can then be used to compute the Bayes factor of FBG node j with respect to unassigned case M (here we assume that for M_K known FBG nodes, $j = 1, ..., N_K$ correspond to the known FBG nodes and $j = M_K + 1, ..., M$ correspond to the unassigned cases. The Bayes factor for case j then is

$$B_{i,j} = \frac{p(\tilde{w}_{t,i} - w_{t-1,j}, \tilde{p}_{t,i} - r_{m,j}(\widetilde{FWHM}_{t,i})|j)}{p(\tilde{w}_{t,i} - w_{t-1,M}, \tilde{p}_{t,i} - r_{m,M}(\widetilde{FWHM}_{t,i})|M)}. \qquad (18)$$

We assume that the prior model is independent of measurement model

$$B_{i,j} = \frac{p(\tilde{w}_{t,i} - w_{t-1,j}|j) p(\tilde{p}_{t,i} - r_{m,j}(\widetilde{FWHM}_{t,i})|j)}{p(\tilde{w}_{t,i} - w_{t-1,M}|M) p(\tilde{p}_{t,i} - r_{m,M}(\widetilde{FWHM}_{t,i})|M)}. \qquad (19)$$

We also assume that for an unassigned peak measurement, the measured reflectivity follows a uniform distribution between 0 and 1. Therefore, $p(\tilde{p}_{t,i} - r_{m,M}(\widetilde{FWHM}_{t,i})|M) = 1$. Similarly, we assume that for unassigned peak measurement, the measured peak wavelength follows a uniform distribution over the Interrogator wavelength window, L_{IW}. Therefore, $p(\tilde{w}_{t,i} - w_{t-1,M}|M) = \frac{1}{L_{IW}}$. The simplified Bayes factor is then

$$B_{i,j} = L_{IW} p(\tilde{w}_{t,i} - w_{t-1,j}|j) p(\tilde{p}_{t,i} - r_{m,j}(\widetilde{FWHM}_{t,i})|j). \qquad (20)$$

We also assume that the prior model and measurement models follow normal distributions with standard deviations Q and R

$$p(\tilde{w}_{t,i} - w_{t-1,j}|j) \sim \mathcal{N}\left(0, Q_d^2\right) \qquad (21)$$

$$p(\tilde{p}_{t,i} - r_{m,j}(\widetilde{FWHM}_{t,i})|j) \sim \mathcal{N}\left(0, R^2\right) \qquad (22)$$
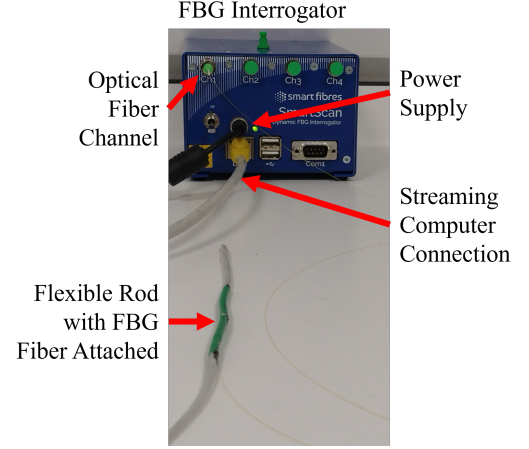

Fig. 4: Experimental setup used for collecting our datasets. A Smartfibres SmartScan interrogator is used to stream spectrum and peak data to a computer which records the dataset. An optical fiber with three FBG nodes is attached to the interrogator's first channel and the FBG nodes are glued to a flexible rod which is then wrapped with heat shrink.

For the process model, note that if a known FBG node has unassigned measurement at $t-1$, then the assignment at $t-2$ (or earlier) must be used and Q must be computed using the propagation of uncertainty function $Q_d = Q\sqrt{\Delta t}$ where Δt is the time difference between the last assigned measurement and the current measurement. Note that the assignment problem minimizes cost and a higher Bayes factor for model j generally implies a better match than model M. Therefore, we simply take the negative of Bayes factors to compute the cost. $c_{i,j} = -B_{i,j}$. Finally, note that for the unassigned models $j = M_K + 1, ..., M$, $c_{i,j} = -1$ by definition.

IV. Experiments

To demonstrate the utility of varying FBG reflectivity and FWHM for shape sensing, as well as to verify our FBG spectra model, detection, and classification method, we collect a series of datasets with an FBG array as shown in Fig. 4. We use a SmartScan interrogator (Smart Fibres Ltd, UK) and an optical fiber with three 4 mm FBGs with center wavelengths of 1538, 1548, and 1558 nm with a tolerance of 0.04 nm, a full width half maximum of 0.6 nm with a 0.05 nm bandwidth tolerance, a reflectivity of 35%, 60%, and 80% with a 5% tolerance, and a side lobe suppression ratio greater than 15 dB. This FBG array was manufactured by Technica Optical Components LLC using an SM1250BI(9.8/125)P optical fiber with polyimide coating. The optical fiber was glued along a flexible plastic tube 2.75 mm in diameter. The tube was then manually bent for several minutes and three datasets were collected. Spectrum messages state the reflected signal intensity (with the default automatic gain tuning turned off) at regular wavelength intervals. Peak messages state the wavelengths of the measured peaks using the interrogator's default process for peak detection and classification.

In subsection IV-A, we evaluate the model with our dataset, and in subsection IV-B, we evaluate our entire method. In sub-
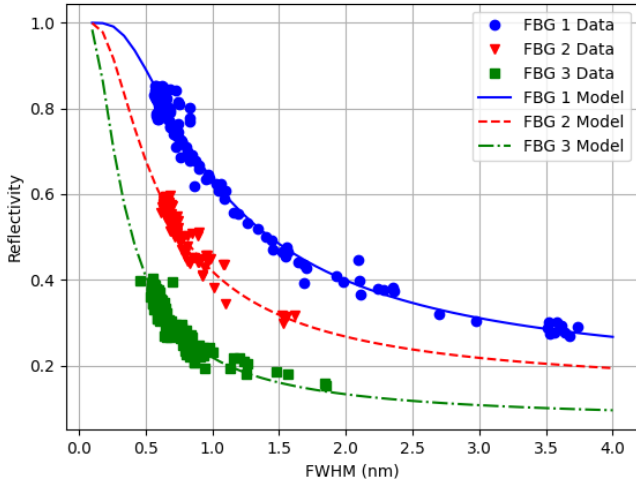
Fig. 5: Hand labeled data and the regressed models for the FBG nodes on the first portion of the dataset. α and β for the first FBG node was found to be 0.2194 and 0.1271 respectively and the covariance matrix of the estimated parameters have a Frobenius norm of 1.045×10^{-5}. For the second node, α and β was found to be 0.1269 and 0.1187 with norm 1.9220×10^{-5}. The third node's α and β was found to be 0.0797 and 0.0817 with norm 1.0334×10^{-5}. The R^2 values for the three models were 0.9753, 0.9072, and 0.9012 for FBG's 1, 2, and 3 respectively.

section IV-C we evaluate our method with specific components removed to show that the model we presented in (16) and the varying reflectivity is an essential component of our method.

A. Evaluating the Model

To evaluate the model expressed in (16), we estimate parameters α and β for each of the three FBG nodes using the first of three collected dataset. Peaks and FWHMs in this case were classified as corresponding to FBG 1, 2, or 3 by hand. Ambiguous cases (a person could not reliably identify which FBG corresponded to which peak) were simply left unlabeled and unused here. In total, 254 points were identified as FBG 1, 249 points were identified as FBG 2, and 275 points were identified as FBG 3. Peaks and FWHM were identified using the same procedure as described in subsections III-B and III-C (with no wavelet-based denoising). Since the interrogator reports reflected intensity values, these are scaled using initial intensity values and reflectivities reported in the optical fiber's datasheet to measure reflectivity. Results are shown in Fig. 5. The data agrees with the regressed models well (with R^2 all above 0.9) and, moreover, there is a clear and visually recognizable difference between the three FBG nodes. This clear difference (due to the chosen reflectivity and FWHM of the three FBG nodes) is what will enable the nodes to be classified by our proposed method.

B. Evaluating the Classification Method

To evaluate the ability of our method to classify FBG nodes, we compute the accuracy, precision, recall, specificity, and

TABLE I: Classification Statistics with our Method and Method used with FBG Interrogator (Test dataset)

	Accuracy	Precision	Recall	Specificity	F_1 Score
FBG 1 (Ours)	0.9911	0.9819	0.9909	0.9912	0.9864
FBG 1 (Int.)	0.8829	0.8951	0.7264	0.9588	0.8020
FBG 2 (Ours)	0.9861	0.9692	0.9875	0.9855	0.9783
FBG 2 (Int.)	0.8542	0.8312	0.6176	0.9432	0.7086
FBG 3 (Ours)	0.9613	1.0	0.8917	1.0	0.9427
FBG 3 (Int.)	0.7798	0.8286	0.4833	0.9444	0.6105
Average (Ours)	0.9795	0.9837	0.9567	0.9922	0.9691
Average (Int.)	0.8390	0.8516	0.6091	0.9488	0.7071

F_1 score for each of the three FBG nodes using the second and third collected datasets. We call the second dataset the validation dataset and permit tuning of hyperparameters (e.g., prominence lower bound, wavelet hard threshold, variance of FBG random walk model, and variance of the model) described in subsections III-B and III-C. We call the third dataset the test dataset and evaluate this only after hyperparameters are tuned. Results for the testing dataset is shown in Table I. Across all measures used on the testing dataset, our proposed approach outperforms the peak detection and classification method used by the commercially available interrogator. In particular, note that the interrogator has a high specificity on our datasets and a relatively low recall. Our proposed method on the other hand has comparable specificity and recall.

C. Evaluating Components of the Classification Method

Our method includes several components (e.g., wavelet-based denoising, a likelihood computed based on a random walk model, etc.) that are not related to our main objective to use differing design FWHM and peak reflectivity to classify measurements using the proposed model in (16). While we believe each of these components are useful for a variety of reasons (for example, prominence-based peak finding speeds up the execution time of the method substantially), we conduct an ablation study in this section to show that the model we presented in (16) and the varying reflectivity is an essential component of our method. Table II shows accuracy, precision, recall, specificity and F_1 score on the testing dataset with different components of the proposed method removed. Across all measures and for all elements removed—except for the use of the FBG model—scores remain above 0.9. When the FBG model is removed, accuracy, recall, and the F_1 score suffer significantly. For example, the F_1 score drops from 0.9691 with the FBG model to just 0.3988.

V. DISCUSSION AND CONCLUSIONS

In this paper, we present a method that can be used to classify FBG nodes on interrogator spectra despite crossing wavelengths, which enables high-resolution sensing at high curvature bendings. The proposed method relies on varying reflectivity and FWHM of FBG nodes along a fiber and using the reflectivity model presented in (16). When compared to a commercially available peak detection and classification system, our method outperforms across all the metrics we considered. We show that this can have useful implications for

TABLE II: Ablation Study of method (Test dataset)

	Accuracy	Precision	Recall	Specificity	F_1 Score
Average (Ours)	0.9795	0.9837	0.9567	0.9922	0.9691
Without Wavelets	0.9798	0.9847	0.9567	0.9927	0.9696
Without Prominence	0.9696	0.9748	0.9373	0.9878	0.9534
Without Prior Model	0.9785	0.9857	0.9520	0.9932	0.9675
Without reflectivity model	0.7811	1.0	0.3257	1.0	0.3988

shape sensing in robots and medical instruments that undergo high curvature bends.

The focus of our experiment is on FBG nodes that have crossed. This is due to the difficulty of establishing ground truth design wavelengths when FBG nodes are closely interfering and fall exactly on top of each other. However, our method classifies wavelength peaks before and after this region. This region corresponds to a small portion of data shown with shaded colour in Fig. 1b. We would need to develop accurate models of how these spectra behave when interfering. While we were not be able to classify closely interfering cases by hand, the method we propose often does assign measured peaks to FBG nodes.

We modelled FBGs assuming a uniform grating. There are several other, smaller effects in FBGs that have been documented that can also cause changes in the relationship between FWHM and reflectivity in practice. One of these effects is apodization [21]. Bending (as opposed to stretching) can also introduce nonlinear effects on FBGs due to the differences in the fiber across its cross-section and activation of cladding coupling modes [26]. This is particularly notable since, in shape sensing, we often expect the FBGs to bend. In future work, we will investigate these effects, particularly during interference and bending. Additionally, as we rely on data to fit FBG nodes to our model, upcoming research should aim for online parameter estimation or derive these values a priori via coupled-mode theory.

REFERENCES

[1] S. K. Sahu, C. Sozer, B. Rosa, I. Tamadon, P. Renaud, and A. Menciassi, "Shape Reconstruction Processes for Interventional Application Devices: State of the Art Progress, and Future Directions," *Frontiers in Robot. and AI*, vol. 8, no. 758411, 2021.

[2] G. Ding, S. Yue, S. Zhang, and W. Song, "Strain - deformation reconstruction of CFRP laminates based on Ko displacement theory," *Nondestructive Testing and Evaluation*, vol. 36, no. 2, pp. 145–157, 2021.

[3] P. Bettini, E. Guerreschi, and G. Sala, "Development and Experimental Validation of a Numerical Tool for Structural Health and Usage Monitoring Systems Based on Chirped Grating Sensors," *Sensors*, vol. 15, no. 1, pp. 1321–1341, 2015.

[4] R. Rohan, K. Venkadeshwaran, and P. Ranjan, "Recent advancements of fiber Bragg grating sensors in biomedical application: a review," *J. of Optics*, Mar 2023.

[5] R. J. Roesthuis, M. Kemp, J. J. van den Dobbelsteen, and S. Misra, "Three-Dimensional Needle Shape Reconstruction Using an Array of Fiber Bragg Grating Sensors," *IEEE/ASME Trans. Mechatron.*, vol. 19, no. 4, pp. 1115–1126, 2014.

[6] S. C. Ryu and P. E. Dupont, "FBG-based shape sensing tubes for continuum robots," in *IEEE Int. Conf. on Robot. and Autom.*, 2014, pp. 3531–3537.

[7] R. J. Roesthuis, S. Janssen, and S. Misra, "On using an array of fiber Bragg grating sensors for closed-loop control of flexible minimally invasive surgical instruments," in *IEEE/RSJ Int. Conf. on Intell. Robots and Syst.*, 2013, pp. 2545–2551.

[8] F. Khan, A. Donder, S. Galvan, F. R. y. Baena, and S. Misra, "Pose Measurement of Flexible Medical Instruments Using Fiber Bragg Gratings in Multi-Core Fiber," *IEEE Sensors J.*, vol. 20, no. 18, pp. 10 955–10 962, 2020.

[9] I. Floris, J. M. Adam, P. A. Calderón, and S. Sales, "Fiber Optic Shape Sensors: A comprehensive review," *Optics and Lasers in Eng.*, vol. 139, p. 106508, 2021.

[10] A. Denasi, F. Khan, K. J. Boskma, M. Kaya, C. Hennersperger, R. Göbl, M. Tirindelli, N. Navab, and S. Misra, "An Observer-Based Fusion Method Using Multicore Optical Shape Sensors and Ultrasound Images for Magnetically-Actuated Catheters," in *IEEE Int. Conf. on Robot. and Autom.*, 2018, pp. 50–57.

[11] F. Alambeigi, S. Aghajani Pedram, J. L. Speyer, J. Rosen, I. Iordachita, R. H. Taylor, and M. Armand, "SCADE: Simultaneous Sensor Calibration and Deformation Estimation of FBG-Equipped Unmodeled Continuum Manipulators," *IEEE Trans. Robot.*, vol. 36, no. 1, pp. 222–239, 2020.

[12] M. Ourak, S. D. Buck, X. T. Ha, O. Al-Ahmad, K. Bamps, J. Ector, and E. V. Poorten, "Fusion of Biplane Fluoroscopy With Fiber Bragg Grating for 3D Catheter Shape Reconstruction," *IEEE Robot. Autom. Lett.*, vol. 6, no. 4, pp. 6505–6512, 2021.

[13] X. T. Ha, D. Wu, M. Ourak, G. Borghesan, A. Menciassi, and E. V. Poorten, "Sensor Fusion for Shape Reconstruction Using Electromagnetic Tracking Sensors and Multi-Core Optical Fiber," *IEEE Robot. Autom. Lett.*, vol. 8, no. 7, pp. 4076–4083, 2023.

[14] C. Shi, S. Giannarou, S.-L. Lee, and G.-Z. Yang, "Simultaneous catheter and environment modeling for Trans-catheter Aortic Valve Implantation," in *IEEE/RSJ Int. Conf. on Intell. Robots and Syst.*, 2014, pp. 2024–2029.

[15] A. Triana, D. Pastor, and M. Varón, "Code Division Multiplexing Applied to FBG Sensing Networks: FBG Sensors Designed as Discrete Prolate Spheroidal Sequences (DPSS-FBG Sensors)," *Journal of Lightwave Technology*, vol. 35, no. 14, pp. 2880–2886, 2017.

[16] ——, "A Code Division Design Strategy for Multiplexing Fiber Bragg Grating Sensing Networks," *Sensors*, vol. 17, no. 11, 2017.

[17] S. Ren, S. Chen, J. Yang, J. Wang, Q. Yang, C. Xue, G. Wang, and M. Huang, "High-efficiency FBG array sensor interrogation system via a neural network working with sparse data," *Optics Express*, vol. 31, no. 5, pp. 8937–8952, Feb 2023.

[18] Y. C. Manie, P.-C. Peng, R.-K. Shiu, Y.-T. Hsu, Y.-Y. Chen, G.-M. Shao, and J. Chiu, "Enhancement of the Multiplexing Capacity and Measurement Accuracy of FBG Sensor System Using IWDM Technique and Deep Learning Algorithm," *J. of Lightwave Technol.*, vol. 38, no. 6, pp. 1589–1603, 2020.

[19] S. Balter, J. W. Hopewell, D. L. Miller, L. K. Wagner, and M. J. Zelefsky, "Fluoroscopically Guided Interventional Procedures: A Review of Radiation Effects on Patients' Skin and Hair," *Radiology*, vol. 254, no. 2, pp. 326–341, 2010.

[20] C. E. Campanella, A. Cuccovillo, C. Campanella, A. Yurt, and V. M. N. Passaro, "Fibre Bragg Grating Based Strain Sensors: Review of Technology and Applications," *Sensors*, vol. 18, no. 9, 2018.

[21] T. Erdogan, "Fiber grating spectra," *J. of Lightwave Technol.*, vol. 15, no. 8, pp. 1277–1294, 1997.

[22] K. R. Coombes, S. Tsavachidis, J. S. Morris, K. A. Baggerly, M.-C. Hung, and H. M. Kuerer, "Improved peak detection and quantification of mass spectrometry data acquired from surface-enhanced laser desorption and ionization by denoising spectra with the undecimated discrete wavelet transform," *Proteomics*, vol. 5, no. 16, pp. 4107–4117, November 2005.

[23] K. R. Coombes, K. A. Baggerly, and J. S. Morris, *Fundamentals of Data Mining in Genomics and Proteomics*. New York, NY: Springer Science Business Media, 2007, ch. Pre-Processing Mass Spectrometry Data, pp. 79–102.

[24] C. H. Papadimitriou and K. Steiglitz, *Combinatorial Optimization: Algorithms and Complexity*. Mineola, NY: Dover Publications, Inc., 1998.

[25] D. F. Crouse, "On Implementing 2D Rectangular Assignment Algorithms," *IEEE Trans. Aerosp. Electron. Syst.*, vol. 52, no. 4, pp. 1679–1696, August 2016.

[26] W. Zhang, X. Lei, W. Chen, H. Xu, and A. Wang, "Modeling of spectral changes in bent fiber Bragg gratings," *Optics Lett.*, vol. 40, no. 14, pp. 3260–3263, Jul 2015.